Journal of Materials Chemistry C

ROYAL SOCIETY OF CHEMISTRY

PAPER

View Article Online
View Journal



Cite this: DOI: 10.1039/d6tc00246c

# Chirality-guided crystal packing for tunable clustering-triggered emission

Zhipeng Zhao,[a] Yueying Lai,[ab] Zhuojie Yin,[a] Xiang Chen,[a] Guangxin Yang,[a] Junhao Duan,[a] Yu Song Cai[a] and Wang Zhang Yuan *[a]

Received 24th January 2026,
Accepted 3rd March 2026

DOI: 10.1039/d6tc00246c

rsc.li/materials-c

Nonconventional luminophores possess unique optical properties governed by the clustering-triggered emission (CTE) mechanism, yet rational regulation of their crystal packing to minimize nonradiative decay remains a significant challenge. Herein, we report a stereochemical engineering strategy to modulate the packing mode and lattice rigidity of imide-based nonconventional luminophores, thereby optimizing their photoluminescence (PL) and persistent room-temperature phosphorescence (p-RTP). Chiral model compounds (*R*/*S*-DIV) and racemic counterparts (*rac*-DIV) were synthesized *via* a straightforward amidation between the imide scaffold and chiral valine. Structural analysis revealed that while the bulky isopropyl group of valine induces steric repulsion and results in less efficient molecular packing within the homochiral lattice, the racemic crystal exhibits a significantly denser, alternating *R*/*S* cross-stacked architecture, consistent with Wallach's rule. This densified packing effectively restricts intramolecular motions and strengthens intermolecular interactions. Consequently, at room temperature, *rac*-DIV exhibits superior photophysical performance, achieving a quantum efficiency ($\Phi_c$) and phosphorescence lifetime ($\tau_p$) approximately 1.5-fold and 4-fold higher, respectively, than those of its homochiral counterparts. These findings validate the pivotal role of stereochemistry in controlling molecular packing and offer a generalizable approach for developing high-performance nonconventional luminophores.



## Introduction

Nonconventional luminophores have emerged as a transformative class of optical materials in recent years,[1–6] circumventing the conventional reliance on extended π-conjugation. In contrast to typical chromophores dependent on large aromatic conjugated frameworks,[7–17] nonconventional chromophores are characterized by abundant electron-rich units, such as heteroatoms,[18–20] rendering their luminescence properties intrinsically sensitive to the aggregation state.[21–23] The clustering-triggered emission (CTE) mechanism posits that through-space conjugation (TSC) within clusters, formed by the aggregation of electron-rich units, facilitates electron delocalization and subsequent emission.[24–26] Notably, conformational rigidity serves as a cornerstone of the CTE mechanism, playing a pivotal role in modulating the photophysical properties of these systems.[27–29] Within loosely packed lattices, pronounced molecular motions facilitate the rapid nonradiative decay of excitons. Consequently, precise engineering of the crystal packing to suppress such dynamic processes and enhance intermolecular rigidity is imperative for optimizing the performance of these materials. While hydrogen and halogen bonding are commonly employed to stabilize molecular packing,[30–32] the utilization of stereochemistry—specifically chirality—as a primary design parameter to modulate packing density and lattice rigidity has received limited attention.

While chiral moieties have been primarily investigated for their capability to induce circularly polarized luminescence (CPL),[33–36] their role in governing molecular packing architectures is of equal significance.[37–39] The inherent structural asymmetry of chiral groups restricts orientational degrees of freedom, thereby directing the spatial arrangement and packing patterns of molecules within the crystalline state.[40–42] By rationally modulating the configuration (*R* or *S*) of these chiral moieties, the packing mode of the crystal lattice can be precisely engineered. This, in turn, regulates the rigidity of the local environment of emissive species through modulating the strength of intermolecular interactions. Inspired by such structural tunability, we systematically explored stereochemical engineering as a strategy to modulate both the photoluminescence (PL) and persistent room-temperature phosphorescence

[a] State Key Laboratory of Synergistic Chem-Bio Synthesis, School of Chemistry and Chemical Engineering, Frontiers Science Center for Transformative Molecules, Shanghai Key Lab of Electrical Insulation and Thermal Aging, Shanghai Jiao Tong University, No. 800 Dongchuan Rd., Minhang District, Shanghai 200240, China. E-mail: wzhyuan@sjtu.edu.cn
[b] School of Chemical Engineering, Xianyang Vocational Technical College, Xianyang, Shaanxi 712000, China

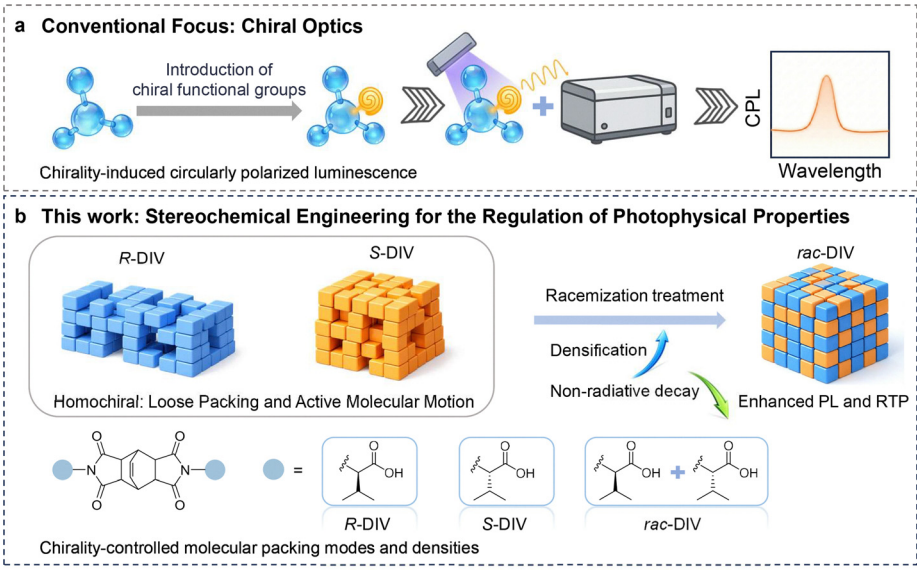


Fig. 1 (a) Application of chiral groups in previous studies. (b) Schematic illustration of the present study, in which the introduction of chiral groups enables regulation of molecular crystal packing modes and density, thereby achieving control over photophysical properties.

(p-RTP) properties of nonconventional luminophores. Model compounds were designed and synthesized through a facile amidation reaction between a common imide core and chiral valine. In this framework, the amino acid side chains function as stereochemical modulators that regulate molecular conformational rigidity *via* steric hindrance effects, thereby dictating the packing modes within the lattice (Fig. 1).

This study elucidates a fundamental structure–property relationship governed by chiral-directed crystal packing and its impact on photophysical modulation. Compared with *N*,*N*′-bis[(*R*)-1-carboxy-2-methylpropyl]naphthalene-1,4,5,8-tetracarboxylic diimide (*R*-DIV), *N*,*N*′-bis[(*S*)-1-carboxy-2-methylpropyl]-naphthalene-1,4,5,8-tetracarboxylic diimide (*S*-DIV) exhibits both a higher crystal PL efficiency ($\Phi_c$) and a longer phosphorescence lifetime ($\tau_p$), primarily owing to its highly ordered molecular packing. However, the bulky isopropyl group intrinsic to the valine moiety induces pronounced steric repulsion within the homochiral lattice, disrupting close intermolecular alignment and resulting in a loosely packed crystalline architecture. Such structural looseness amplifies low-frequency molecular motions, including rotation and vibration, thereby facilitating efficient nonradiative decay pathways. To overcome this limitation and modulate the packing architecture, the racemic variant, *rac*-DIV, was synthesized. In accordance with Wallach's rule, the racemic crystal exhibits a higher density compared to its homochiral counterparts.[43,44] Single-crystal X-ray diffraction analysis reveals that *rac*-DIV adopts a tightly packed, alternating *R*/*S* cross-stacked arrangement—a stark contrast to the more open packing observed in the homochiral crystals. This densified packing significantly strengthens intermolecular interactions and effectively suppresses dynamic lattice disorder. Consequently, at room temperature, *rac*-DIV demonstrates markedly improved photophysical performance, with a $\Phi_c$ and $\tau_p$ approximately 1.5-fold and 4-fold greater, respectively, than those of the homochiral counterparts. This work transcends the conventional design paradigm focused solely on CPL, systematically elucidating the pivotal role of stereochemical engineering in constructing high-density, rigidified molecular packings. These findings demonstrate that the rational incorporation of chiral moieties serves as an effective strategy to modulate the emission properties of purely organic luminescent systems, and provides design guidance for developing high-performance nonconventional luminophores.

## Results and discussion

### Photophysical properties of enantiopures and *rac*-DIV crystals at room temperature

The successful synthesis of DIV molecules is corroborated by proton ($^1$H) and carbon ($^{13}$C) nuclear magnetic resonance (NMR) spectroscopy (Fig. S1 and S2). Under 312 nm UV irradiation, all DIV crystals exhibit blue-violet emission. Upon cessation of excitation, distinct green p-RTP is observed (Fig. 2a). Although visual differences are indiscernible to the naked eye, their PL spectra reveal significant disparities. *R*-DIV crystals display emission peaks at 348, 378, 395, and 510 nm, whereas *S*-DIV crystals exhibit a dominant peak at approximately 395 nm accompanied by a shoulder near 428 nm. Notably, compared to *S*-DIV, the prompt PL spectrum of *R*-DIV reveals a more pronounced shoulder at approximately 510 nm (Fig. 2b), indicating a higher contribution from triplet excitons. In contrast, the prompt PL spectrum of the racemate, *rac*-DIV, displays multiple sharp peaks at 375, 411, 438, and 463 nm, likely arising from the coexistence of both enantiomers and associated intermediates. With a delay time ($t_d$) of 0.1 ms, the emission maxima for *R*- and *S*-DIV crystals are located at 527 nm and 523 nm, respectively, attributable to their p-RTP emissions. Measurements of the

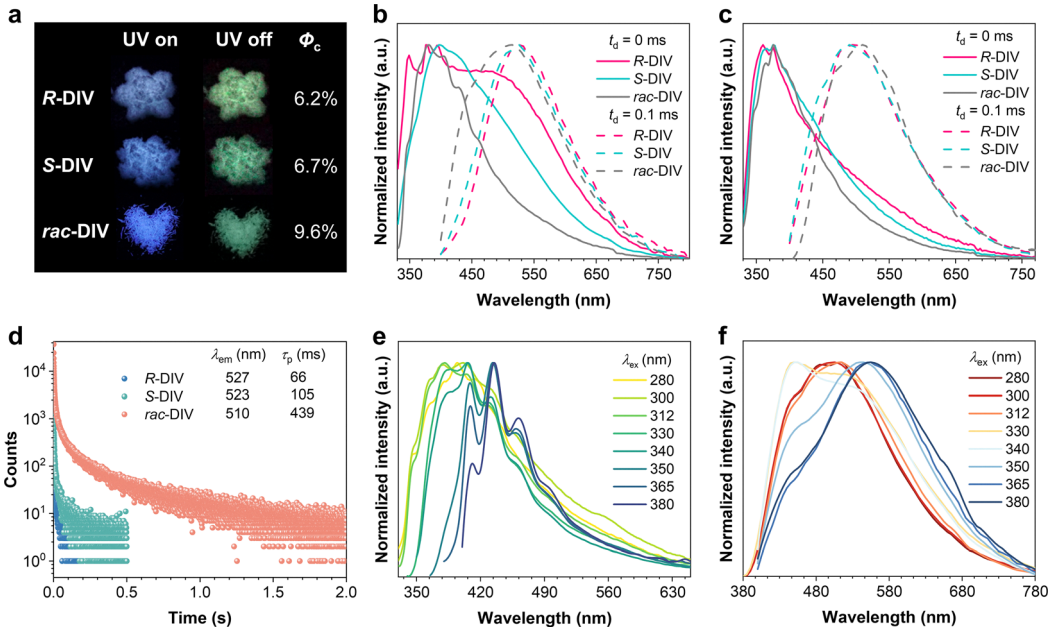


Fig. 2 (a) Photographs and PL quantum efficiencies of DIV crystals under 312 nm irradiation and after cessation. (b) and (c) Prompt and delayed ($t_d$ = 0.1 ms) PL spectra of (b) DIV crystals and (c) their ground solids ($\lambda_{ex}$ = 312 nm). (d) RTP decay profiles of DIV crystals ($\lambda_{ex}$ = 312 nm). (e) Prompt and (f) delayed ($t_d$ = 0.1 ms) PL spectra of *rac*-DIV crystals under varying $\lambda_{ex}$s.

absolute $\Phi_c$ and $\tau_p$ yield values of 6.2% and 66 ms for *R*-DIV, and 6.7% and 105 ms for *S*-DIV (Fig. 2a and d). Furthermore, the delayed emission spectrum of *rac*-DIV also presents a multi-peak profile centered at 450 and 510 nm (Fig. 2b), accompanied by a distinctly broader lifetime distribution (Fig. S7), further supporting the presence of multiple emitting species. Importantly, *rac*-DIV crystals exhibit a superior $\Phi_c$ (9.6%) and a substantially prolonged $\tau_p$ (439 ms) (Fig. 2a and d), suggesting that its molecular packing architecture is more effective in suppressing nonradiative transitions and enhancing PL performance.

Mirror-image circular dichroism (CD) signals of $10^{-3}$ M aqueous solutions of *R*- and *S*-DIV (Fig. S3) confirm the successful transfer of the amino acid-derived chiral centers to the final products, forming enantiopure molecular structures. Conversely, the CD spectrum of the *rac*-DIV shows no significant signal fluctuations near the baseline, indicating a lack of overall optical activity, consistent with the mutual cancellation of the *R* and *S* configurations. We attribute the distinct PL performance among the DIV crystals to packing differences induced by their chiral configurations. To validate this hypothesis, crystals of *R*-, *S*-, and *rac*-DIV are ground into powders and vacuum-dried. The results show that, after grinding, the normalized prompt and delayed PL spectral profiles of the three samples tend towards uniformity, showing significantly increased similarity (Fig. 2c). Specifically, in the prompt emission spectra, powders of *R*-, *S*-, and *rac*-DIV all exhibit emission peaks at 358 nm and 376 nm, with narrowed full width at half maximum (FWHM) compared to their pristine crystalline states. In the delayed spectra, the primary emission peaks for *R*- and *S*-DIV are located at 490 nm, while that of *rac*-DIV is at 510 nm, retaining some minor differences. Notably, the PL emission peaks of the ground DIV powders exhibit a slight blue shift relative to the pristine crystals (Fig. 2b and c). This hypsochromic shift likely originates from grinding-induced cluster reconfiguration, leading to a relative increase in the proportion of cluster species dominated by short-wavelength emission. These findings indicate that while the intrinsic luminescent characteristics of the material are largely retained after lattice destruction, the ordered molecular packing architecture directed by chirality in the pristine crystals plays a pivotal role in modulating the photophysical properties.

### Photophysical properties of enantiopures and *rac*-DIV crystals at low temperature

All three DIV crystals exhibit excitation wavelength ($\lambda_{ex}$)-dependent PL emission at room temperature (Fig. 2e, f and Fig. S5–S7), a characteristic feature of nonconventional luminophores.[45–47] Upon lowering the temperature to 77 K, the PL intensity of the DIV crystals is significantly enhanced (Fig. 3 and Fig. S9–S11), the spectral shapes of the three variants tend to converge, and the proportion of phosphorescence components increases markedly (Fig. 3a). Furthermore, at low temperature, *rac*-DIV displays four distinct PL emission peaks at 375, 411, 438, and 463 nm (Fig. 3a), consistent with the room-temperature positions, but with altered relative intensities. These peaks encompass the primary emission features of both *R*- and *S*-DIV, further suggesting the presence of multiple structurally similar emissive clusters within both the enantiomers and the racemate. Notably, at 77 K, the phosphorescence emission peaks for both the enantiomers and the racemate appear around 480 nm, exhibiting a significant blue shift compared to room temperature (Fig. 2b and 3a). Concurrently,

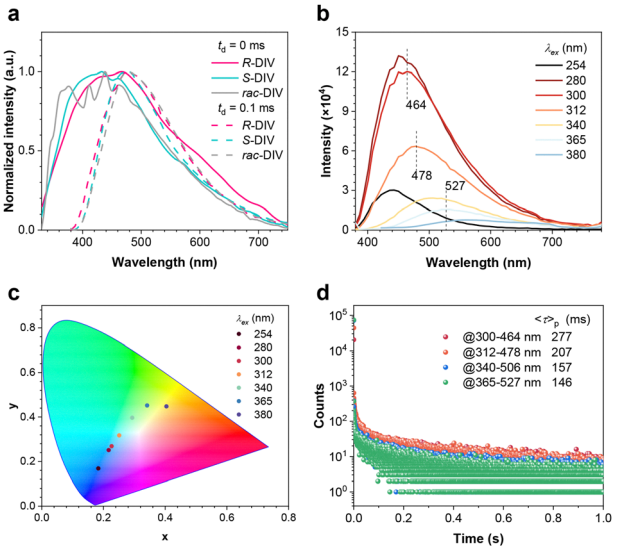


Fig. 3 (a) Prompt and delayed ($t_d$ = 0.1 ms) emission spectra of *R*-DIV, *S*-DIV and *rac*-DIV at 77 K. (b) Delayed ($t_d$ = 0.1 ms) PL spectra, (c) CIE coordinate diagram and (d) lifetime profiles of *R*-DIV at 77 K.

the $\tau_p$ values of the *R*-DIV, *S*-DIV, and *rac*-DIV crystals are significantly prolonged, reaching 207, 291, and 462 ms, respectively (Fig. 3d and Fig. S10, S11). These results indicate that the effective suppression of molecular motion in a low-temperature environment significantly enhances the emission originating from smaller cluster species.

Additionally, at 77 K, DIV crystals retain their $\lambda_{ex}$-dependent PL emission characteristics, with the low-temperature phosphorescence showing even greater sensitivity to the $\lambda_{ex}$ (Fig. 3 and Fig. S10, S11). Under low-temperature conditions, the delayed emission behaviors of *R*-DIV, *S*-DIV, and *rac*-DIV crystals exhibit high similarity (Fig. 3a). Taking *R*-DIV as an example, when $\lambda_{ex}$ is tuned from 280 to 365 nm, its primary p-RTP emission peak redshifts from 520 to 560 nm, with the emission color remaining confined to the yellow-green region (Fig. S5). This subtle chromatic change renders the differences indiscernible to the naked eye, indicating a very limited tunable color range. In contrast, at 77 K, as $\lambda_{ex}$ increases from 254 to 380 nm, the phosphorescence peak gradually redshifts from 443 to 560 nm, and the emission color evolves correspondingly from blue ($\lambda_{ex}$ = 254 nm) to cyan ($\lambda_{ex}$ = 312 nm), and then to yellow ($\lambda_{ex}$ = 380 nm). The CIE chromaticity coordinates shift almost linearly, moving sequentially from (0.183, 0.169) to (0.251, 0.317), and finally reaching (0.404, 0.448) (Fig. 3c). The high consistency in delayed spectral shapes and emission colors among the three crystal types contrasts sharply with their significantly different $\tau_p$ values, suggesting that while the cluster emission centers possess similar structural features, their local packing environments differ. Specifically, subtle variations in molecular packing modulate the relative population of these aggregate species and their local microenvironments, ultimately leading to variations in PL intensity and lifetimes. Notably, the low-temperature $\tau_p$ of *rac*-DIV remains far superior to that of its homochiral counterparts, mirroring the room-temperature trend (Fig. S11). This reconfirms that the racemic system likely possesses a tighter crystal packing structure that is more conducive to suppressing nonradiative decay.

## Single-crystal structures and molecular packing

To gain deeper insights into the PL properties of the aforementioned crystals, their single-crystal structures are determined. As illustrated in Fig. 4 and Tables S1–S4, the *R*-DIV crystal crystallizes in the monoclinic $P2_1$ space group, whereas the *S*-DIV crystal adopts the triclinic *P*1 space group. These chiral crystals possess asymmetric structures composed of homochiral molecules. In stark contrast, the racemic *rac*-DIV crystal is optically inactive and crystallizes in the centrosymmetric *C*2/*c* space group. In *R*-DIV, isopropyl groups adopt a *trans* disposition across the molecular plane, producing a pronounced lateral steric barrier. This symmetry can bias the lattice toward higher-symmetry packing; however, steric blockage from the bulky groups limits close intermolecular engagement, leading to scattered, discontinuous short contact motifs. Nevertheless, the intramolecular O═C···C═C interactions (2.883–2.994 Å) within the *R*-DIV molecule effectively extend its conjugation[48] (Fig. S12). Concurrently, abundant C═O···O–H contacts (2.655–2.709 Å) synergistically facilitate the formation of triplet excitons in aggregated chromophores *via* TSC. Furthermore, a rigid network established by short contacts, such as C═O···H–O (1.874–2.082 Å) and C═O···H–C (2.497–2.717 Å), significantly enhances molecular conformational rigidity (Fig. 4a). This structural rigidification is pivotal for suppressing nonradiative transitions, boosting PL efficiency, and stabilizing triplet excitons, thereby enabling significant dual fluorescence-phosphorescence emission at room temperature.

In *S*-DIV, the isopropyl groups are situated on the same side of the molecular plane. This *cis*-orientation breaks the inherent geometric symmetry of the molecule, inducing it to crystallize in the *P*1 space group. Such an asymmetric packing environment creates unique polar voids, which actively capture lattice water molecules. Compared to the lateral shielding and discrete contact motifs in *R*-DIV—arising from the *trans*-orientation of its isopropyl groups—the *cis*-conformation-driven and water-mediated multicenter hydrogen-bonding network in *S*-DIV constructs a more robust three-dimensional rigid environment. Specifically, the C═O···H–C interaction distances in the *S*-DIV crystal are significantly shortened (2.416–2.700 Å), and the bond length distributions for C═O···O–H contacts and C═O···H–O hydrogen bonds exhibit enhanced uniformity (Fig. 4b). This multi-level structural rigidification more effectively suppresses the nonradiative transition pathways of excited-state clusters, thereby endowing *S*-DIV with a higher $\Phi_c$ and a longer $\tau_p$. The *rac*-DIV crystal exhibits a pronounced increase in the number of intermolecular interactions (Fig. 4c). *R*- and *S*-DIV molecules are arranged in a mirror-symmetric fashion on opposite sides of a lamellar structure, forming an ordered layered packing stabilized by multiple hydrogen bonds. Scanning electron microscopy (SEM) results further demonstrate that the enantiopure DIV crystals exhibit a rod-like morphology, whereas the racemic crystals display a platelet-like structure (Fig. 4d).

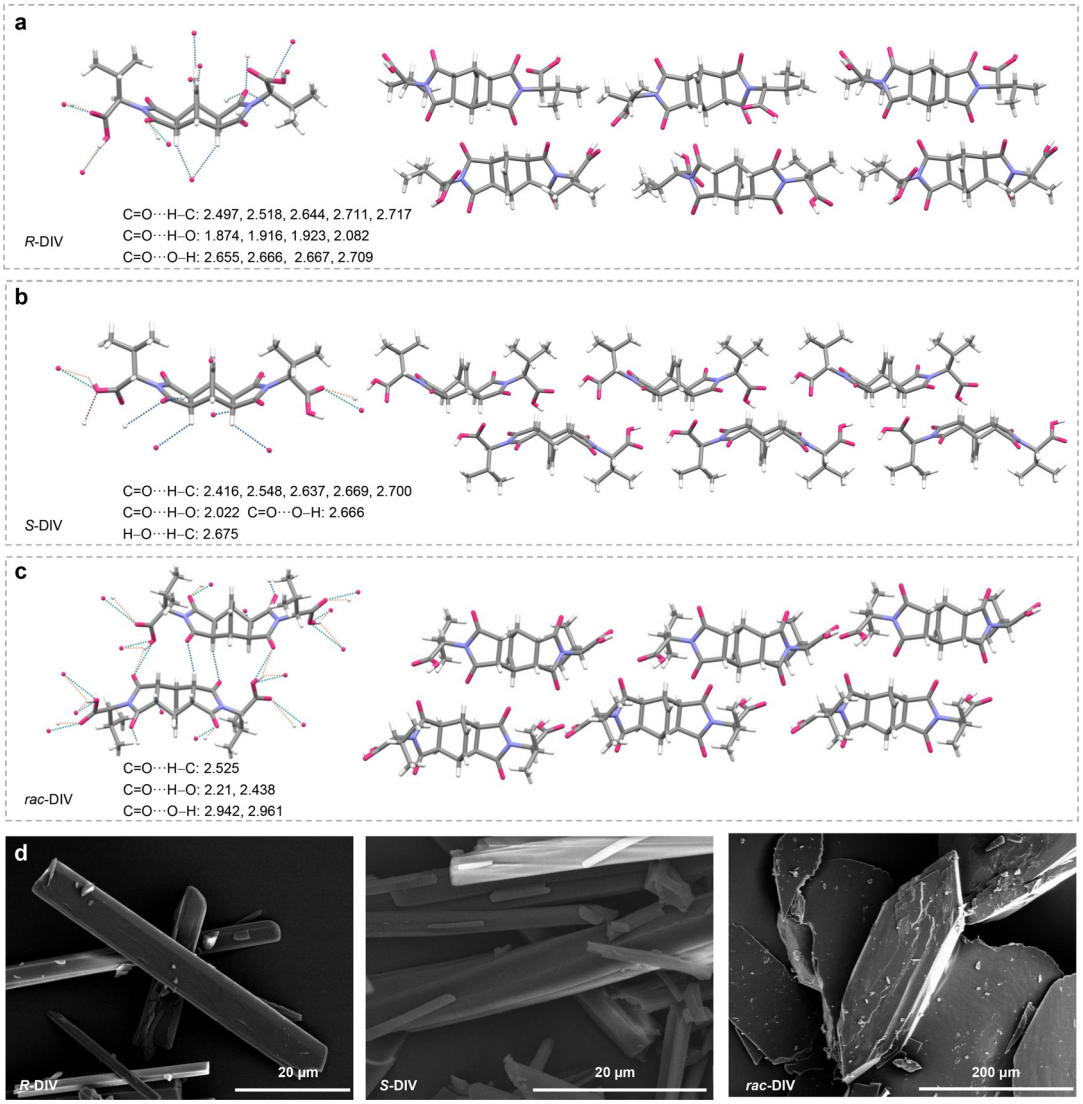


Fig. 4 Single-crystal structures and packing of (a) *R*-DIV, (b) *S*-DIV, and (c) *rac*-DIV. (d) SEM images of *R*-DIV, *S*-DIV, and *rac*-DIV. The intermolecular interactions are indicated by dashed lines: C═O···H–C (blue), C═O···O–H (green), C═O···H–O (yellow), and H–O···H–C (purple).

Benefiting from higher structural symmetry and regularity, *rac*-DIV achieves a tighter molecular packing (1.420 g $cm^{-3}$). This significantly strengthens both intramolecular and intermolecular interactions, thereby yielding $\Phi_c$ and $\tau_p$ values superior to those of the corresponding enantiomers. Moreover, the fractional free volume of the *rac*-DIV crystal is lower than that of its enantiomers, further corroborating its more compact molecular packing mode (Fig. S13 and S14).

Electrostatic potential (ESP)[49–51] analysis reveals that the *rac*-DIV dimer exhibits the highest degree of electrostatic complementarity, characterized by the effective overlap between electron-deficient (blue) and electron-rich (red) regions (Fig. 5a). In contrast, the homochiral dimers, particularly *R*-DIV, display less favorable electrostatic matching with potential repulsive contacts. The stronger intermolecular interactions within *rac*-DIV facilitate the formation of a more rigid crystal lattice, which effectively suppresses nonradiative decay pathways of the emissive clusters, resulting in superior PL performance. To further elucidate the noncovalent interactions within the crystal lattices, interaction region indicator (IRI)[52] analyses were performed (Fig. 5b). The results demonstrate that the *rac*-DIV dimer exhibits the most continuous and broad green isosurfaces between adjacent molecules, indicative of extensive and uniform van der Waals interactions. This suggests that the heterochiral stacking mode maximizes the intermolecular contact area, thereby achieving a highly compact and rigid molecular arrangement. Conversely, the interaction regions in the homochiral dimers (*S*-DIV and *R*-DIV) appear more dispersed and fragmented. Subsequently, the highest occupied molecular orbital (HOMO) and lowest unoccupied molecular orbital (LUMO) energy levels of the *R*-DIV, *S*-DIV, and *rac*-DIV dimers were calculated (Fig. 5c). The results indicate that *rac*-DIV and the *S*-DIV exhibit a stronger tendency for electron delocalization compared to the *R*-DIV, a phenomenon closely correlated

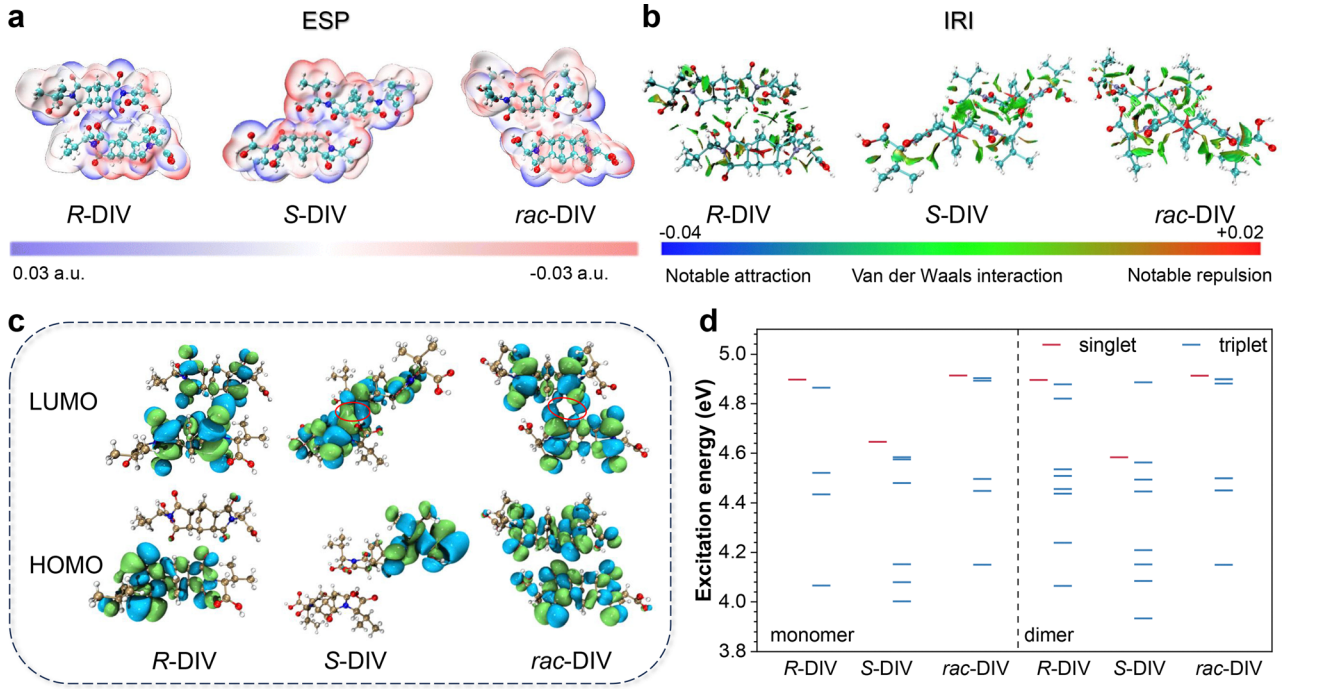


Fig. 5 Electrostatic potential spectra (a) and interaction region indicator analysis (b) of *R*-DIV, *S*-DIV, and *rac*-DIV. (c) Electron densities of the HOMO and the LUMO of *R*-DIV, *S*-DIV and *rac*-DIV dimers. (d) Comparison of the excitation energy diagrams of *R*-DIV, *S*-DIV and *rac*-DIV monomers and dimers.

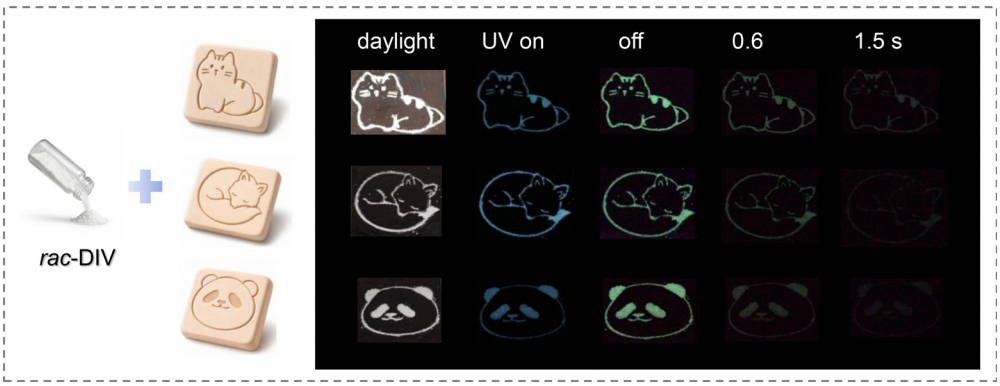


Fig. 6 Anti-counterfeiting applications utilizing *rac*-DIV crystals.

with their denser molecular packing. Furthermore, as the degree of aggregation increases, the $S_1$ and $T_1$ energy levels of both enantiomers and the racemate gradually decrease (Fig. 5d). This trend facilitates effective exciton delocalization, thereby enhancing the emission efficiency of both PL and RTP.

Owing to the exceptionally high $\Phi_c$ demonstrated by *rac*-DIV crystals, their application was extended to the fabrication of anti-counterfeiting patterns. As illustrated in Fig. 6, *rac*-DIV crystals were cast into molds with predefined patterns, enabling the preparation of shape-specific anti-counterfeiting features. Upon irradiation with a 312 nm UV lamp, all three patterns exhibited intense blue-violet fluorescence. Following removal of the excitation source, a pronounced green RTP emission was clearly observed from each pattern.

## Conclusions

In summary, this work represents a paradigm shift in the crystal engineering of nonconventional luminophores, redefining chirality as a pivotal parameter for modulating molecular packing mode rather than merely a source of optical activity. Through the precise manipulation of the stereochemical configuration of chiral building blocks, effective control over crystal packing modes and molecular density was attained, enabling the rational tuning of the photophysical properties. The enantiopure crystals, governed by the stereochemical configuration of their chiral moieties, typically adopt distinct polymorphic structures characterized by highly constrained molecular arrangements—resulting in an intrinsically low packing density.

In stark contrast, within the racemic *rac*-DIV crystal, the *R*- and *S*-enantiomers form a tightly cross-stacked architecture, facilitating a significantly higher crystal packing density (1.42 g $cm^{-3}$). This densification of the crystal lattice effectively restricts intra and intermolecular motions, thereby rigidifying the cluster environment and suppressing nonradiative decay pathways. Consequently, *rac*-DIV exhibits superior optical performance, achieving a $\Phi_c$ of 9.6% and a $\tau_p$ of 439 ms. This study not only enhances the understanding of structure–property relationships in nonconventional luminophores, but also demonstrates stereochemical control as a promising approach for designing highly rigid and efficient solid-state emissive materials.

## Conflicts of interest

There are no conflicts to declare.

## Data availability

The data supporting this article have been included as part of the supplementary information (SI). Supplementary information: additional experimental details, extended methods, supplementary figures and tables supporting the findings of this study. See DOI: https://doi.org/10.1039/d6tc00246c.

CCDC 2524918 (*R*-DIV), 2524919 (*S*-DIV) and 2524920 (*rac*-DIV) contain the supplementary crystallographic data for this paper.[53a–c]

## Acknowledgements

This work was financially supported by the National Natural Science Foundation of China (U22A20250 and 52473185), the Project of State Key Laboratory of Synergistic Chem-Bio Synthesis (SKLSCBS202552) and the Project of Opening Project of Shanghai Key Laboratory of Crime Scene Evidence (2024XCWZK05).

## Notes and references

1 M. Mahapatra, M. Bourguignon, P. Stiernet, S. Melo, B. Grignard, M. Vandevenne, M. Galleni and C. Detrembleur, *Adv. Funct. Mater.*, 2025, e23095.
2 N. Jiang, H. Zhang and M. R. Bryce, *Trends Chem.*, 2025, **7**, 603–616.
3 X. Chen, S. Tao, R. Chen, Z. Zhao, Q. Zhang, A. Li, G. Yang, W. Liu and W. Z. Yuan, *Mater. Horiz.*, 2026, **13**, 1412–1420.
4 Q. Zhang, Z. Zhao, G. Yang, A. Li, Y. Cui, Y. Cai, Z. Yin, Y. Tan, C. Zhou, Q. Peng and W. Z. Yuan, *Adv. Funct. Mater.*, 2025, **35**, 2423603.
5 Y. Zhao, L. Xu, Y. He, Z. Feng, W. Feng and H. Yan, *Aggregate*, 2024, **5**, e471.
6 L. Guo, L. Yan, Y. He, W. Feng, Y. Zhao, B. Z. Tang and H. Yan, *Angew. Chem., Int. Ed.*, 2022, **61**, e202204383.
7 G. Yang, S. Hao, Y. Dan, L. Dang, H. Zhang, Q. Zhang, A. Li, M.-D. Li and W. Z. Yuan, *Adv. Mater.*, 2025, **37**, 2418042.
8 Z. Zhao, Y. Bi, Y. Wu, Z. Wang, H. Liu, C. Du, H. Yuan, D. Ding, H. Ou and Y. Tan, *Nano Lett.*, 2025, **25**, 8547–8557.
9 N. Gan, X. Zou, Z. Qian, A. Lv, L. Wang, H. Ma, H. J. Qian, L. Gu, Z. An and W. Huang, *Nat. Commun.*, 2024, **15**, 4113.
10 L. Zhou, J. Song, Z. He, Y. Liu, P. Jiang, T. Li and X. Ma, *Angew. Chem., Int. Ed.*, 2024, **63**, e202403773.
11 Y. Yang, Y. Qi, A. Li, Y. Shan, Z. Chen, M. Shan, X. Du, K. Wang, K. Yang, B. Z. Tang and Z. Li, *Adv. Mater.*, 2026, e18840.
12 Z. Xie, H. Deng, X. Ge, Z. Chi and B. Liu, *J. Am. Chem. Soc.*, 2025, **147**, 12722–12729.
13 C. Ren, Z. Wang, H. Ou, T. Wang, Z. Zhao, Y. Wei, H. Yuan, Y. Tan and W. Z. Yuan, *Small Methods*, 2024, **8**, 2300243.
14 T. Wang, Z. Wang, Z. Li, Z. Chen, H. Sun, H. Yuan, H. Ou, X. Huang and Y. Tan, *Chem. Eng. J.*, 2024, **495**, 153026.
15 R. Du, Z. Wang, Z. Zhao, H. Liu, S. Jiao, Y. Wu, W. Li, H. Yuan, H. Ou and D. Ding, *Mater. Chem. Front.*, 2025, **9**, 2752–2762.
16 Y. Wu, Z. Zhao, S. Jiao, T. Song, C. Du, B. Fan, Y. Pang, H. Yuan and H. Ou, *Biomed. Technol.*, 2025, **11**, 100098.
17 Z. Zhao, R. Du, X. Feng, Z. Wang, T. Wang, Z. Xie, H. Yuan, Y. Tan and H. Ou, *Curr. Med. Chem.*, 2025, **32**, 322–342.
18 D. Wang and T. Imae, *J. Am. Chem. Soc.*, 2004, **126**, 13204–13205.
19 Q. Fan, Y. Tang, H. Sun, D. Guo, J. Ma and J. Guo, *Adv. Mater.*, 2024, **36**, 2401315.
20 C.-Y. Shi, D.-D. He, B.-S. Wang, Q. Zhang, H. Tian and D.-H. Qu, *Angew. Chem., Int. Ed.*, 2023, **62**, e202214422.
21 J. Deng, H. Liu, D. Liu, L. Yu, Y. Bai, W. Xie, T. Li, C. Wang, Y. Lian and H. Wang, *Adv. Funct. Mater.*, 2023, **34**, 2308420.
22 H. Ju, H. Zhang, L. X. Hou, M. Zuo, M. Du, F. Huang, Q. Zheng and Z. L. Wu, *J. Am. Chem. Soc.*, 2023, **145**, 3763–3773.
23 J. Deng, D. Liu, H. Liu, L. Yu, Y. Bai, J. Xiao and H. Wang, *Adv. Funct. Mater.*, 2024, **34**, 2408821.
24 Q. Zhou, B. Cao, C. Zhu, S. Xu, Y. Gong, W. Z. Yuan and Y. Zhang, *Small*, 2016, **12**, 6586–6592.
25 H. Zhang, Z. Zhao, P. R. McGonigal, R. Ye, S. Liu, J. W. Y. Lam, R. T. K. Kwok, W. Z. Yuan, J. Xie, A. L. Rogach and B. Z. Tang, *Mater. Today*, 2020, **32**, 275–292.
26 Z. Zhao, A. Li and W. Z. Yuan, *Acc. Chem. Res.*, 2025, **58**, 612–624.
27 B. He, J. Zhang, J. Zhang, H. Zhang, X. Wu, X. Chen, K. H. S. Kei, A. Qin, H. H. Y. Sung, J. W. Y. Lam and B. Z. Tang, *Adv. Sci.*, 2021, **8**, 2004299.
28 Y. Wang, Y. Zhao, X. Chen, T. Li, X. Zhang, J. Huang, J. Qiao and W. Dong, *Macromolecules*, 2025, **58**, 354–362.
29 L. He, X. Nan, T. Wang, Z. Liu, C. Wang, T. Gu and P. Bai, *Aggregate*, 2025, **6**, e70176.
30 T. Zhu, T. Yang, Q. Zhang and W. Z. Yuan, *Nat. Commun.*, 2022, **13**, 2658.
31 R. Zhou, X. Lu, X. Zhou, X. Liu, S. Wang, T. Y. Ohulchanskyy, D.-C. Yin and J. Qu, *Aggregate*, 2025, **6**, e70070.
32 M. Yi, P. Qi, Q. Fan and J. Hao, *J. Mater. Chem. C*, 2022, **10**, 1645–1652.

33 J. Zhang, S. Zhang, C. Sun, R. Wang, Z. Guo, D. Cui, G. Tang, D. Li, J. Yuan, X. Lu, C. Zheng, W. Huang and R. Chen, *Adv. Mater.*, 2025, **37**, 2500953.
34 D. Liu, W.-J. Wang, P. Alam, Z. Yang, K. Wu, L. Zhu, Y. Xiong, S. Chang, Y. Liu, B. Wu, Q. Wu, Z. Qiu, Z. Zhao and B. Z. Tang, *Nat. Photonics*, 2024, **18**, 1276–1284.
35 S. Garain, S. Sarkar, B. Chandra Garain, S. K. Pati and S. J. George, *Angew. Chem., Int. Ed.*, 2022, **61**, e202115773.
36 H. Li, J. Gu, Z. Wang, J. Wang, F. He, P. Li, Y. Tao, H. Li, G. Xie, W. Huang, C. Zheng and R. Chen, *Nat. Commun.*, 2022, **13**, 429.
37 W. Xiao, K.-H. Ernst, K. Palotas, Y. Zhang, E. Bruyer, L. Peng, T. Greber, W. A. Hofer, L. T. Scott and R. Fasel, *Nat. Chem.*, 2016, **8**, 326–330.
38 W. Ji, B. Xue, S. Bera, S. Guerin, L. J. W. Shimon, Q. Ma, S. A. M. Tofail, D. Thompson, Y. Cao, W. Wang and E. Gazit, *Mater. Today*, 2021, **42**, 29–40.
39 X. Wu, C.-Y. Huang, D.-G. Chen, D. Liu, C. Wu, K.-J. Chou, B. Zhang, Y. Wang, Y. Liu, E. Y. Li, W. Zhu and P.-T. Chou, *Nat. Commun.*, 2020, **11**, 2145.
40 S. E. Penty, M. A. Zwijnenburg, G. R. F. Orton, P. Stachelek, R. Pal, Y. Xie, S. L. Griffin and T. A. Barendt, *J. Am. Chem. Soc.*, 2022, **144**, 12290–12298.
41 Y. Zhang, Y. Liu, W. Jiang and Z. Wang, *Acc. Mater. Res.*, 2025, **6**, 158–171.
42 Q. Zhang, R. Toyoda, L. Pfeifer and B. L. Feringa, *J. Am. Chem. Soc.*, 2023, **145**, 6976–6985.
43 C. Peng Qiu, M. Luo Xi, J. Qin Yu, T. Wang, B. Bai, L. Wei Xi, K. Li and Q. Zang Shuang, *CCS Chem.*, 2022, **4**, 3686–3692.
44 W. Wang, J. Gong, J. Zhao, H. Zhang, W. Wen, Z. Zhao, Y. J. Li, J. Wang, C. Z. Huang and P. F. Gao, *Adv. Sci.*, 2024, **11**, 2403249.
45 Y. S. Cai, Z. Wang, Y. Cui, X. Chen, G. Yang, H. Ou, H. Yuan and W. Z. Yuan, *Adv. Mater.*, 2025, e18820.
46 X. Ji, W. Tian, K. Jin, H. Diao, X. Huang, G. Song and J. Zhang, *Nat. Commun.*, 2022, **13**, 3717.
47 C. Shang, Y. Zhao, J. Long, Y. Ji and H. Wang, *J. Mater. Chem. C*, 2020, **8**, 1017–1024.
48 Y. Lai, T. Zhu, T. Geng, S. Zheng, T. Yang, Z. Zhao, G. Xiao, B. Zou and W. Z. Yuan, *Small*, 2020, **16**, 2005035.
49 T. Lu and F. Chen, *J. Comput. Chem.*, 2012, **33**, 580–592.
50 T. Lu, *J. Chem. Phys.*, 2024, **161**, 082503.
51 T. Lu and F. Chen, *J. Mol. Graphics Modell.*, 2012, **38**, 314–323.
52 T. Lu and Q. Chen, *Chem. Methods*, 2021, **1**, 231–239.
53 (*a*) CCDC 2524918: Experimental Crystal Structure Determination, 2026, DOI: 10.5517/ccdc.csd.cc2qrczv; (*b*) CCDC 2524919: Experimental Crystal Structure Determination, 2026, DOI: 10.5517/ccdc.csd.cc2qrd0x; (*c*) CCDC 2524920: Experimental Crystal Structure Determination, 2026, DOI: 10.5517/ccdc.csd.cc2qrd1y.